EUMETSAT

AC SAF

ATMOSPHERIC COMPOSITION
MONITORING

ALGORITHM THEORETICAL BASIS DOCUMENT

GOME-2 Absorbing Aerosol Height

Product Identifier	Product Name	
O3M-68, O3M-69	AAH from GOME-2 / MetOp-A	(NRT, offline)
O3M-78, O3M-79	AAH from GOME-2 / MetOp-B	(NRT, offline)
O3M-364, O3M-365	AAH from GOME-2 / MetOp-C	(NRT, offline)
O3M-170	AAH from GOME-2 / MetOp-A/B/C	(DR)

L.G. Tilstra	Royal Netherlands Meteorological Institute (KNMI)
O.N.E. Tuinder	Royal Netherlands Meteorological Institute (KNMI)
P. Wang	Royal Netherlands Meteorological Institute (KNMI)
P. Stammes	Royal Netherlands Meteorological Institute (KNMI)

Document status sheet

Issue	Date	Page(s)	Modified Items / Reason for Change
1.0	11-02-2016	all	first version of document
1.1	08-12-2017	all	added two more case studies to section 3.1 ; update
1.2	08-02-2018	all	changes to section 1, 2, and 3 ; update after RR/PCR
1.3	23-02-2018	all	further changes after RR/PCR
1.4	02-04-2019	8,30	added new section 1.3 ; updated appendix A
1.5	21-05-2021	15	updated section 2.5

Contents

Introduction to EUMETSAT Satellite Application Facility on Atmospheric Composition monitoring (AC SAF)

Background

The monitoring of atmospheric chemistry is essential due to several human caused changes in the atmosphere, like global warming, loss of stratospheric ozone, increasing UV radiation, and pollution. Furthermore, the monitoring is used to react to the threads caused by the natural hazards as well as follow the effects of the international protocols.

Therefore, monitoring the chemical composition and radiation of the atmosphere is a very important duty for EUMETSAT and the target is to provide information for policy makers, scientists and general public.

Objectives

The main objectives of the AC SAF is to process, archive, validate and disseminate atmospheric composition products (O_3, NO_2, SO_2, BrO, HCHO, H_2O, OClO, CO, NH_3), aerosol products and surface ultraviolet radiation products utilising the satellites of EUMETSAT. The majority of the AC SAF products are based on data from the GOME-2 and IASI instruments onboard MetOp satellites.

Another important task besides the near real-time (NRT) and offline data dissemination is the provision of long-term, high-quality atmospheric composition products resulting from reprocessing activities.

Product categories, timeliness and dissemination

NRT products are available in less than three hours after measurement. These products are disseminated via EUMETCast, WMO GTS or internet.

- Near real-time trace gas columns (total and tropospheric O_3 and NO_2, total SO_2, total HCHO, CO) and ozone profiles
- Near real-time absorbing aerosol indexes from main science channels and polarisation measurement detectors
- Near real-time UV indexes, clear-sky and cloud-corrected

Offline products are available within two weeks after measurement and disseminated via dedicated web services at EUMETSAT and AC SAF.

- Offline trace gas columns (total and tropospheric O_3 and NO_2, total SO_2, total BrO, total HCHO, total H_2O) and ozone profiles
- Offline absorbing aerosol indexes from main science channels and polarisation measurement detectors
- Offline surface UV, daily doses and daily maximum values with several weighting functions

Data records are available after reprocessing activities from the EUMETSAT Data Centre and/or the AC SAF archives.

- Data records generated in reprocessing
- Surface Lambertian-equivalent reflectivity
- Total OClO

Users can access the AC SAF offline products and data records (free of charge) by registering at the AC SAF web site.

More information about the AC SAF project, products and services: http://acsaf.org/

AC SAF Helpdesk: helpdesk@acsaf.org

Twitter: https://twitter.com/Atmospheric_SAF

1   Introduction

1.1   Document purpose and scope

This document is the Algorithm Theoretical Basis Document (ATBD) for the GOME-2 Absorbing Aerosol Height (AAH) product developed at KNMI in the framework of the AC SAF (Satellite Application Facility on Atmospheric Composition Monitoring). The aim of this ATBD is to present the scientific background of the algorithm and to provide a description of the algorithm setup.

1.2   Heritage

The GOME-2 AAH product is a brand new product. However, it uses the Absorbing Aerosol Index (AAI) product produced by the AC SAF [*Tilstra et al.*, 2010] for aerosol detection, and the part of the AAH algorithm code that derives the actual height of the absorbing aerosol layer using the O_2-A band is derived from the FRESCO+ cloud information algorithm [*Wang et al.*, 2008].

1.3   GOME-2 AAH products

The GOME-2 AAH products are created in NRT and offline processing, from the level-1 data generated from the GOME-2 instruments onboard the MetOp-A, MetOp-B, and MetOp-C satellites. Next to this, a GOME-2 AAH data record based on data from all three MetOp satellites will also be produced. An overview of the data products and allocated product identifiers is given in Table 1.

Product ID	Satellite	Platform	Type
O3M-68	GOME-2	MetOp-A	NRT
O3M-69	GOME-2	MetOp-A	offline
O3M-78	GOME-2	MetOp-B	NRT
O3M-79	GOME-2	MetOp-B	offline
O3M-364	GOME-2	MetOp-C	NRT
O3M-365	GOME-2	MetOp-C	offline
O3M-170	GOME-2	MetOp-A/B/C	DR

Table 1: Overview of the AAH offline and NRT data products and data records that are produced, and the product identifiers that are currently allocated to the products and datarecords.

1.4   Abbreviations and acronyms

AAH	Absorbing Aerosol Height
AAI	Absorbing Aerosol Index
AC SAF	Satellite Application Facility on Atmospheric Composition Monitoring
AOT	Aerosol Optical Thickness
ATBD	Algorithm Theoretical Basis Document
BBA	Biomass Burning Aerosol
BRDF	Bidirectional Reflectance Distribution Function
BSA	Black-Sky Albedo
CDOP	Continuous Development & Operations Phase
COT	Cloud Optical Thickness
DAK	Doubling-Adding KNMI
DDA	Desert Dust Aerosols
DOAS	Differential Optical Absorption Spectroscopy
DU	Dobson Units, 2.69×10^{16} molecules cm^{-2}
ENVISAT	Environmental Satellite
EOS-Aura	Earth Observing System – Aura satellite
ERS	European Remote Sensing Satellite
ESA	European Space Agency
ETOPO-4	Topographic & Bathymetric data set from the NGDC, 4 arc-min. resolution
EUMETSAT	European Organisation for the Exploitation of Meteorological Satellites
FOV	Field-of-View
FRESCO	Fast Retrieval Scheme for Clouds from the Oxygen A band
FWHM	Full Width at Half Maximum
GMTED2010	Global Multi-resolution Terrain Elevation Data 2010
GOME	Global Ozone Monitoring Experiment
HDF	Hierarchical Data Format
IT	Integration Time
KNMI	Koninklijk Nederlands Meteorologisch Instituut
LER	Lambertian-Equivalent Reflectivity
LUT	Look-Up Table
MERIS	Medium Resolution Imaging Spectrometer
METOP	Meteorological Operational Satellite
MLS	Mid-Latitude Summer
MSC	Main Science Channel
NGDC	NOAA's National Geophysical Data Center (Boulder, Colorado, USA)

NISE	Near-real-time Ice and Snow Extent
NOAA	National Oceanic and Atmospheric Administration
NRT	Near-Real-Time
OMI	Ozone Monitoring Instrument
O3M SAF	Satellite Application Facility on Ozone and Atmospheric Chemistry Monitoring
PMD	Polarisation Measurement Device
PSD	Product Specification Document
PUM	Product User Manual
RMSE	Root-Mean-Square Error
RTM	Radiative Transfer Model
SCIAMACHY	Scanning Imaging Absorption Spectrometer for Atmospheric Chartography
SZA	Solar Zenith Angle
TEMIS	Tropospheric Emission Monitoring Internet Service
TOA	Top-of-Atmosphere
TOMS	Total Ozone Mapping Spectrometer
UTC	Coordinated Universal Time
UV	Ultraviolet
VIS	Visible
VR	Validation Report
VZA	Viewing Zenith Angle

2   Algorithm setup

2.1   Introduction

The algorithm used to derive the AAH is based on earlier work published in *Wang et al.* [2012]. In this paper, the possibility of retrieving absorbing aerosol layer height using an adapted version of the FRESCO+ cloud retrieval algorithm was investigated. The outcome of the study was very positive. Inspired by this work, the AAH algorithm introduced in this ATBD is closely related to the FRESCO+ cloud retrieval algorithm [*Wang et al.*, 2008], but also uses the GOME-2 AAI product [*Tilstra et al.*, 2010] as input. The next section will provide an overview of the algorithm setup.

2.2   Algorithm description

The algorithm is designed to handle GOME-2 level-1b PDUs. First, however, the associated AAI level-2 PDU is opened and each observation in it is examined. Observations with solar zenith angles larger than 85 degrees are skipped and the AAH is returned as not determined. Observations in sun glint geometries are likely to be affected by sun glint and are skipped (see section 2.4). Observations known to be affected by a solar eclipse event are also skipped (see section 2.5). Whenever the AAI is below 4, the amount of absorbing aerosol is too small to result in a reliable retrieval of the AAH. In this case the observation is skipped and the AAH is returned as not determined. If the AAI value is higher than 4, then the algorithm will try to retrieve aerosol layer height in the following way.

In order to simulate the reflectance spectrum of a partly aerosol containing pixel inside and outside the O_2-A band, a simple atmospheric model is used, in which the atmosphere above the ground surface (for the clear-sky part of the pixel) and above the aerosol layer (for the aerosol/cloud containing part of the pixel) is treated as an absorbing (due to oxygen) and purely Rayleigh scattering medium. Reflection occurs only at the surface and the top of the aerosol layer. Surface and aerosol/cloud layer are both assumed to be Lambertian reflectors. The reflectance $R_{sim}(\lambda, \theta, \theta_0, \phi - \phi_0)$ at wavelength λ, viewing zenith angle θ, solar zenith angle θ_0, and relative azimuth angle $\phi - \phi_0$ is then given by

$$R_{sim} = c \cdot T_c(z_c) \cdot A_c + c \cdot R_c(z_c) + (1 - c) \cdot T_s(z_s) \cdot A_s + (1 - c) \cdot R_s(z_s) . \qquad (1)$$

If $c = 1$, the surface related terms vanish and equation (1) is simplified to

$$R_{sim} = T_c(z_{sc}) \cdot A_{sc} + R_c(z_{sc}) . \qquad (2)$$

Note that the wavelength and directional dependencies are omitted in equations (1) and (2) for R_{sim}, T_c, R_c, T_s, and R_s. In the above equations, c is the effective aerosol/cloud cover fraction at the O_2-A band, A_c is the albedo of the aerosol/cloud layer, A_s is the surface albedo, and A_{sc} is the scene

albedo. The terms $T(\lambda, z_{\text{s}}, \theta, \theta_0)$, $T(\lambda, z_{\text{c}}, \theta, \theta_0)$, and $T(\lambda, z_{\text{sc}}, \theta, \theta_0)$ are the direct atmospheric transmittances for light entering the atmosphere from the solar direction, propagating down to different levels characterised by surface height z_{s}, aerosol/cloud height z_{c}, and scene height z_{sc}, respectively, then propagating to the top of the atmosphere (TOA) in the direction of the satellite. Oxygen absorption and single Rayleigh scattering are both taken into account in the light paths for the transmittances and in the single Rayleigh scattering reflectances above the aerosol/cloud layer (R_{c}) and the surface (R_{s}), respectively, in the way as described in, for instance, *Wang et al.* [2008]. The transmittances and reflectances are pre-calculated and stored in a look-up table (LUT).

The GOME-2 AAH algorithm essentially retrieves aerosol layer height using two approaches. In the first approach, equation (1) is used, and the aerosol/cloud layer height z_{c} is retrieved along with effective aerosol/cloud cover fraction c. The aerosol layer albedo A_{c} is set to a fixed value of 0.8, which is an appropriate value for clouds [*Koelemeijer et al.*, 2001; *Wang et al.*, 2008] and also a functional value for thick aerosol layers [*Wang et al.*, 2012]. The parameters retrieved this way are in fact identical to the parameters retrieved by the FRESCO+ cloud information retrieval.

In the second approach, the scene albedo A_{sc} and scene height z_{sc} are derived using equation (2), i.e., by assuming the aerosol/cloud fraction c to be equal to one [*Koelemeijer et al.*, 2001; *Stammes et al.*, 2008; *Wang et al.*, 2008]. Large aerosol plumes often cover several GOME-2 pixels. Thus, it seems reasonable to assume an aerosol/cloud cover fraction of one in these situations. The scene height z_{sc} can be very different than the aerosol/cloud height z_{c}, as will be explained in section 2.3.

In the AAH algorithm, the aerosol/cloud height, scene height and surface height are converted to aerosol/cloud pressure, scene pressure and surface pressure using the standard Mid-Latitude Summer (MLS) atmosphere [*Anderson et al.*, 1986]. Therefore, in the AAH products the terms "height" and "pressure" are interchangeable. Heights and pressure will both be available in the end product. Auxiliary databases that are needed by the AAH algorithm are the GOME-2A surface albedo product [*Tilstra et al.*, 2017] and the GMTED2010 surface height database [*Danielson and Gesch*, 2011].

In summary, the AAH algorithm retrieves, from the level-1b PDU, the following parameters:

– CF: effective aerosol/cloud fraction c

– CH: aerosol/cloud height z_{c}

– SA: scene albedo A_{sc}

– SH: scene height z_{sc}

Two different aerosol/cloud layer heights (z_{c} and z_{sc}) are determined by the AAH algorithm. It is up to the algorithm to decide which of the two is the best candidate to represent the actual AAH. The basis for doing this is and the reliability of the outcome are discussed in the next section.

2.3   Sensitivity study

This section summarises some of the results from the sensitivity study presented in *Wang et al.* [2012]. According to this study the above algorithm is not only able to determine the height of an absorbing aerosol layer in the absence of clouds, but under certain conditions also in the presence of clouds. This is explained in Figures 1 and 2. In both figures some of the results of the sensitivity study are presented. In the study, the four parameters CF, CH, SA, and SH are retrieved from simulated O_2-A band reflectance spectra. The four parameters are presented on the vertical axes in Figures 1 and 2.

In the simulations, an aerosol layer is located in the model atmosphere between a certain height range (indicated in the plot windows). In Figure 1 the aerosol layer consists of biomass burning aerosol (BBA), while Figure 2 presents the case of elevated dust aerosol. On the horizontal axes the AOT (at 760 nm and 340 nm) of the aerosol layer is presented. Below the aerosol layer a thick cloud layer (COT = 20) is present. The simulations are performed for two sets of solar zenith angles ($\theta_0 = 30°$ and $\theta_0 = 60°$). The black data points represent the cases that were described so far, the red data points describe the same cases but then without the cloud layer present in the model atmosphere.

From the two figures the following conclusions can be drawn. For scenes *without* clouds (red data points), the retrieved CH is representative for the aerosol layer height, but the SH is generally not. Only for very high AOT is the SH representative for the aerosol layer height. So, for cloud-free scenes the parameter to trust is the CH. The associated retrieved CF is below $\sim$0.25. For scenes *with* clouds (black data points), the retrieved CH and SH are only representative for the aerosol layer height in case of a very high AOT. The algorithm therefore starts by looking if the AAI is higher than the threshold value 4.0. Only if it is will the AAH be retrieved by the AAH algorithm.

Next, The AAH algorithm retrieves the parameters CF, CH, SA, and SH. To determine whether CH or SH should be reported as the AAH, the algorithm distinguishes three situations (regimes):

A:	CF $\leq$ 0.25	$\rightarrow$	AAH = CH	(high reliability)
B:	0.25 < CF < 0.75	$\rightarrow$	AAH = max(SH,CH)	(medium reliability)
C:	CF $\geq$ 0.75	$\rightarrow$	AAH = CH	(low reliability)

The effective cloud fraction (CF) is used to check in which of these regimes inside the parameter space the solution is likely to be found. The scheme is based on the results of the study presented in *Wang et al.* [2012] (and in Figures 1 and 2). Regime A (CF $\leq$ 0.25) refers to the situation in which there is only a low degree of cloud cover (red data points in the "CF vs AOT" plot) or if the AOT is sufficiently large to compensate the presence of a cloud layer below the aerosol layer (black data points with CF $\leq$ 0.25 in the "CF vs AOT" plot). In this case the results reported in *Wang et al.* [2012] clearly show that the cloud height (CH) is close to the real height of the aerosol layer in almost all
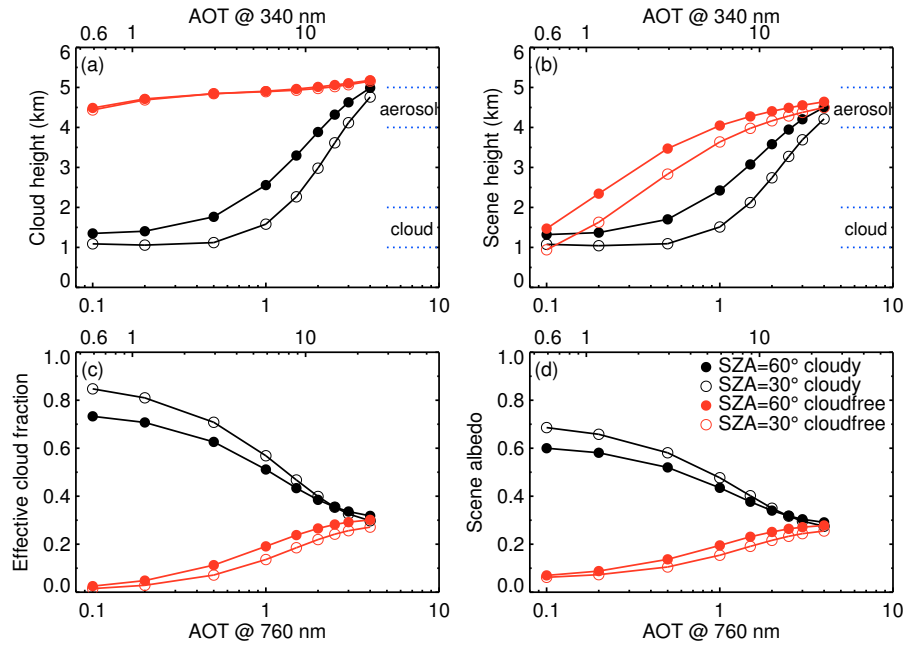
Figure 1: Retrieval results of (a) aerosol/cloud height, (b) scene height, (c) effective aerosol/cloud fraction, and (d) scene albedo using simulated O_2-A band spectra for biomass burning aerosol in a cloud-free scene (red) and in a cloudy scene (black). The cloud layer is located between 1 and 2 km altitude and the aerosol layer between 4 and 5 km. The aerosol optical thickness (AOT) ranges between 0 and 4. The surface albedo A_s is 0.05 and the viewing zenith angle θ is 0°.
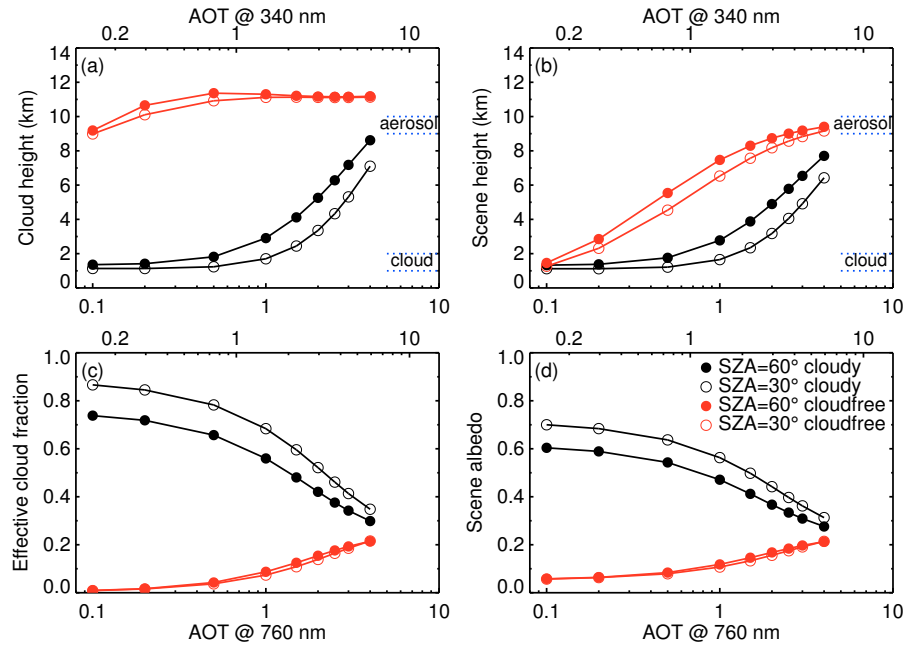
Figure 2: Similar to Figure 1 but now calculated for an aerosol layer containing dust aerosol (instead of biomass burning aerosol). The aerosol layer is now located between 9 and 10 km.

cases. Exceptions are cases with low aerosol amounts, but these scenes were filtered out beforehand by demanding that the AAI must be higher than the threshold value of 4.0 index points.

Regime C (CF $\geq$ 0.75) is the situation of a thick cloud layer present in the scene. In this case, an aerosol layer is only retrieved successfully when the aerosol layer is sufficiently thick. According to the results presented in *Wang et al.* [2012], the best value for the AAH is that of the cloud height (CH). In most cases, however, the AAH is severely underestimated. The reliability is therefore characterised as "low". Finally, regime B (0.25 < CF < 0.75) is an intermediate regime, and the best estimate is the highest value from cloud height (CH) and scene height (SH). The AAH found this way is likely to underestimate the AAH in some cases, and the reliability attributed to this regime is "medium".

All of this can be deduced from figures 1–3 and 5–7 from the paper by *Wang et al.* [2012].

2.4   Sun glint

Sun glint causes several problems. The primary and most direct problem of sun glint is that it results in of abnormally high values for the AAI. Already this is reason enough to skip scenes affected by sun glint. The second reason for excluding pixels which are likely to be affected by sun glint is that the parameters CF, CH, SA, and SH are not reliable for such cases. This is because the surface reflection of the (Lambertian) surface in the simulations does not include specular reflection.

The sun glint flag provided in the GOME-2 AAI product [*Tuinder and Tilstra*, 2016] is used to filter out potential sun glint cases. We only process pixels with sun glint flag values of 0 or 1. Allowing only sun glint flag values 0 and 1 basically means that sun glint is filtered out only over the oceans when the sun glint angle is smaller than 18 degrees. Doing so, we make use of a more strict condition than advised in the PUM of the AAI product. This is to be on the safe side.

2.5   Solar eclipse events

Solar eclipse events lead to abnormally low values for the retrieved Earth radiance and for the derived Earth reflectance. Following the methodology described in [*Trees et al.*, 2020] we implemented a correction for the Earth radiance for observations that were affected by a solar eclipse. This correction is depending on location, time and wavelength. The data are flagged in the output when a solar eclipse event occurs. An overview of recent solar eclipse events is provided in Tables 2 and 3 of Appendix A.

3 Verification

The verification in this section is performed by comparison with data from the CALIOP lidar instrument onboard the CALIPSO satellite, and by comparison with the MISR Plume Height product.

3.1 Comparison with CALIOP

Being a 532-nm lidar system, the CALIOP instrument onboard the CALIPSO satellite is ideally suited for reliable inspection of the vertical profile below the satellite, all the way down to the Earth's surface if any cloud layers in the scene are not too thick. To be more specific, CALIOP can tell us at which height one or more layers of cloud and/or aerosol particles are located in the atmosphere, and also if such layers are mainly consisting of cloud particles or aerosols. As CALIOP is a lidar instrument, measurements can be performed on the day and night side of the Earth. The downside is that it is not easy to find collocations, because of the narrow orbit track that is scanned.

The CALIOP images that were used were taken from the following website:

https://www-calipso.larc.nasa.gov/products/lidar/browse_images/production/

The following cases with strong aerosol events were studied:

– Kasatochi volcanic eruption

– Mount Kelut volcanic eruption

– Dust storm over West China

– Smoke from forest fires in North America

– Smoke from forest fires in Australia

The above cases are perhaps not the most interesting cases to look at, but they do offer a fair degree of spatial and temporal collocation with the CALIOP measurements.

3.1.1 Case I: Kasatochi volcanic eruption

The Kasatochi volcanic eruption took place on 7 August 2008. The volcano is located on one of the Aleutian Islands (52.17°N, 175.51°W) and has its summit 314 m above sea level. The ash plume resulting from the Kasatochi eruption was well captured by the GOME-2 AAI, as well as by many other GOME-2 products. In Figure 3 the top row presents a global image of the AAI field observed on 8 August 2008, along with a second plot which presents the AAI above the threshold of 4.0 index points for the region of interest (the area surrounding the Kasatochi volcano).
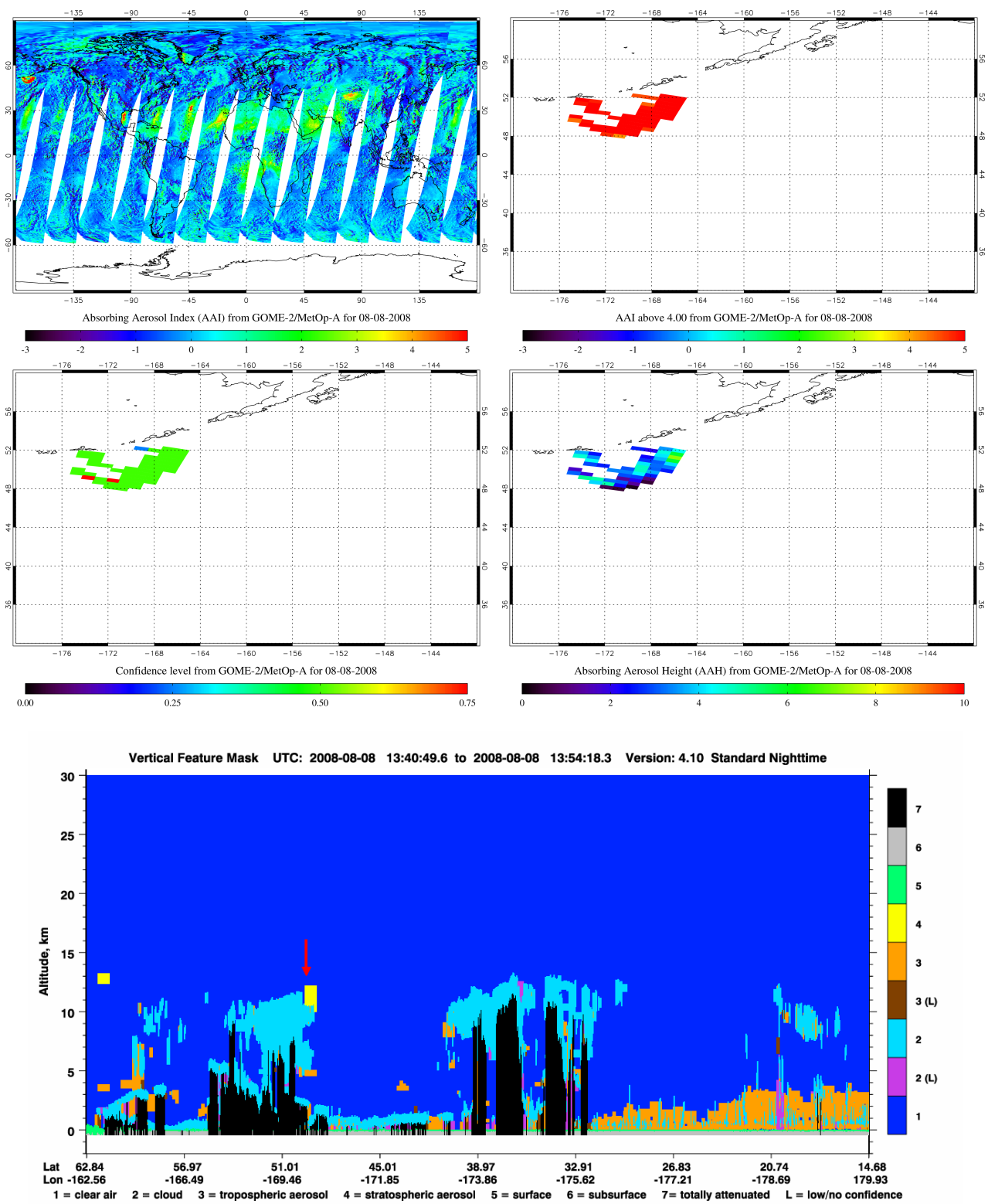
Figure 3: Top row: Images of global AAI and of regional AAI above a threshold value of 4.0 index points. Data are from 8 August 2008. Middle row: Image of AAH and confidence level. Bottom row: CALIOP vertical feature mask. The arrow indicates the relevant geographical location.

The threshold of 4.0 index points in the second plot was selected to indicate the ash plume more clearly. As explained in section 2.2, the AAH algorithm will process all pixels with an AAI of 4.0 index points or higher. The middle row of Figure 3 presents the retrieved AAH (right) and the reliability as defined in section 2.2 (left). The AAH values that are found range from 3 to 6 km. In the bottom row of Figure 3 we present the CALIOP vertical feature mask, which can be found following the URL provided earlier. The arrow indicates the position along the CALIOP orbit track which coincides best with the ash plume as recorded by GOME-2.

The CALIOP vertical feature mask shown in Figure 3 reports an aerosol layer of type "3" at a height of about 5 km. Notice, however, that CALIOP also detects a stratospheric aerosol layer of type "4" above this aerosol layer. The aerosol layer heights reported by the GOME-2 AAH (3–6 km) appear to be address the aerosol layer of type "3", not the higher one of type "4". However, because of the time difference between the GOME-2 and CALIOP overpasses (more than 7 hours time difference) it is more than likely that the small stratospheric plume observed by CALIOP was not observed by GOME-2 simply because it wasn't there anymore. Finding both a proper spatial and temporal collocation with CALIOP is difficult and as the collocation is far perfect it limits the conclusion that may be drawn from this comparison. For the future validation of the GOME-2 AAH product we therefore propose to use trajectory/dispersion models to handle this problem.

3.1.2   Case II: Mount Kelut volcanic eruption

The volcanic eruption of Mount Kelut started on 13 February 2014. In Figure 4 the top row presents a global image of the AAI field observed on 14 February 2014, along with a second plot which presents the AAI above the threshold of 4.0 index points for the region of interest (the area surrounding the Indonesian volcano). The middle row of Figure 4 presents the retrieved AAH. The values that are found range from 8 to 15 km, depending on the position inside the plume. In the bottom row of Figure 4 we present the CALIOP vertical feature mask. The arrow indicates the position along the CALIOP orbit track which coincides best with the ash plume as recorded by GOME-2.

The CALIOP vertical profile indicates that the aerosol plume consists of at least two layers. The lower one is located between 12–15 km and co-exists with a cloud deck, whereas the higher plume is located at a height of ∼19 km. This is higher than the 10–15 km claimed by the AAH retrieval. It should be noted that the highest possible height reported by the AAH retrieval is 15 km, because the look-up tables that are used only go up to this level. Also note the time difference between the GOME-2B and CALIOP overpasses. Taking all this into consideration, we conclude that there is a satisfactory agreement between the GOME-2 AAH and the CALIOP height profile.

Finally, we note that an interesting news item about the Mount Kelut volcanic eruption and the observation of this event by the CALIOP instrument can be found via the following URL:
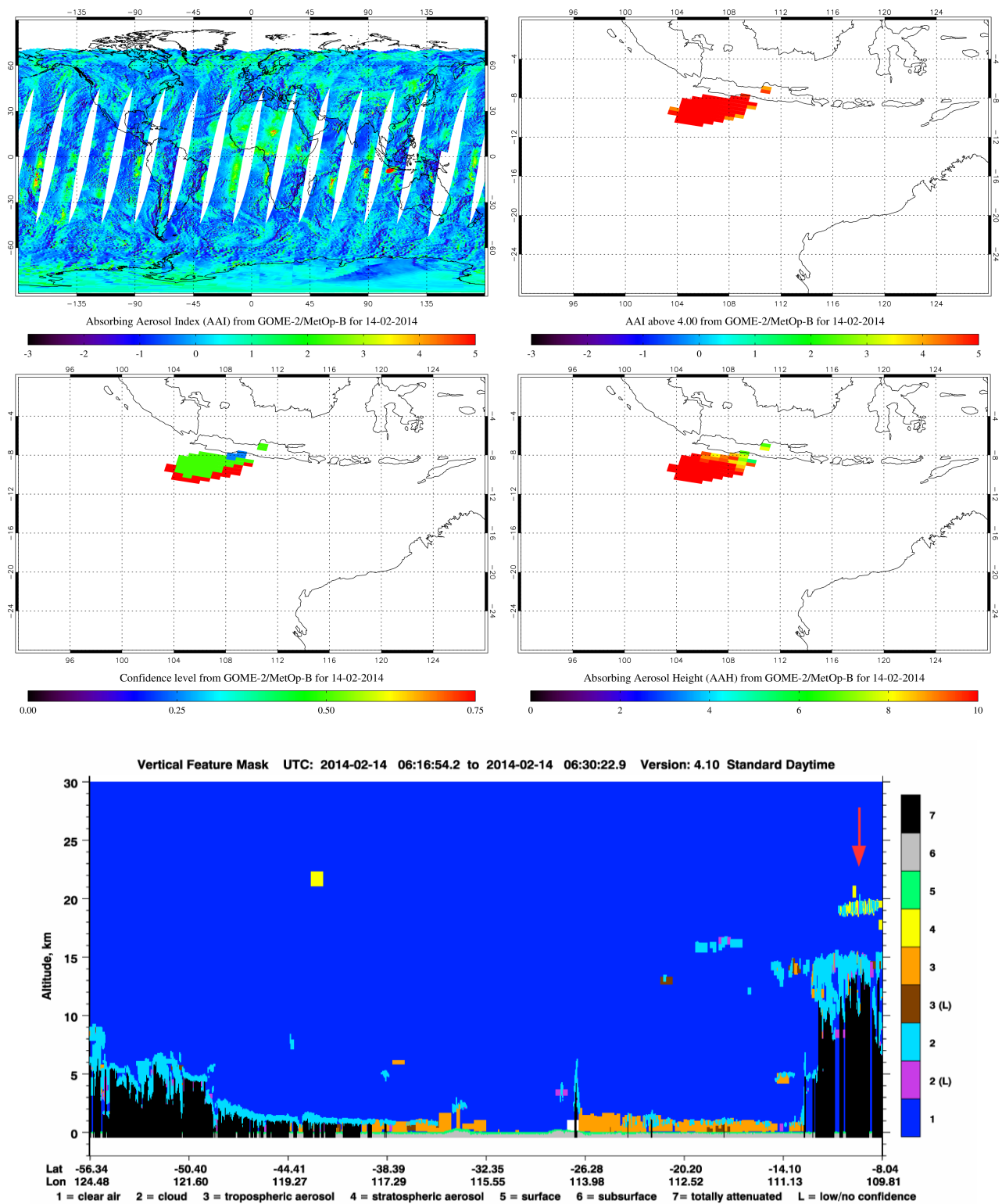
Figure 4: Top row: Global image of AAI and image of regional AAI above a threshold value of 4.0 index points. Data are from 14 February 2014. Middle row: Image of AAH and confidence level. Bottom row: CALIOP vertical feature mask. The arrow indicates the relevant geographical location.

https://earthobservatory.nasa.gov/IOTD/view.php?id=83144&eocn=image&eoci=related_image

It should be noted that here the reported plume heights are even larger. For the plume height nearly 20 km is reported, with some layers even reaching 30 km. The time of measurement quoted in the news item was around 18:10 UTC (nighttime), while we used a CALIOP overpass time around 06:16 (daytime, see Figure 4). However, this is not the explanation. The official CALIOP vertical feature mask mentions for this particular measurement plume heights between 13 and 19 km.

3.1.3   Case III: Dust storm over West China

In Figure 5 the case of a dust storm over West China is presented, in the same format as before. The dust storm was recorded on 24 April 2014, and is in no way exceptional or extreme, but it is interesting because it offers a decent spatial and temporal collocation with the measurements of the CALIOP instrument. The top row of Figure 5 presents the global AAI image and the more regional image of AAI above a threshold of 4.0 index points.

The plot of the retrieved GOME-2 AAH product is shown in the middle row of Figure 5, and the CALIOP vertical feature mask in the bottom row. The arrow in the CALIOP vertical feature mask indicates the point along the orbit track at which there is a fair collocation with the dust plume found in the AAI. The AAH product reports absorbing aerosol layer heights ranging between 1 and 3 km, while from the CALIOP image we find several aerosol layers on top of each other, between 1 and 4 km. These numbers seem to be in line with each other.

3.1.4   Case IV: Smoke from forest fires in North America

The third case we study is the case of smoke from forest fires in North America. The images are presented Figure 6, in the same manner as before. The data presented were recorded on 6 August 2014, but the forest fires had already occurred before this date. In the regional AAI plot (upper row, second plot) the forest fires are located in the left lower tail of the smoke plume. The smoke travelled north, then bent towards the east while climbing and ended up above the Hudson Bay, where the collocation with the CALIOP orbit track took place.

The AAH plot (middle row) shows that the smoke plume reached altitudes between 5 and 8 km above the Hudson Bay. In the CALIOP vertical feature mask (bottom row) we find the aerosol layer to be located at heights ranging between 5 and 9 km. This is quite a good agreement between the GOME-2 AAH product and the CALIOP vertical feature mask. Note that the CALIOP results are very reliable, but that the collocation between the GOME-2 orbit swath and CALIOP orbit track is never perfect in both space and time. Nevertheless, the results from the comparison are encouraging.
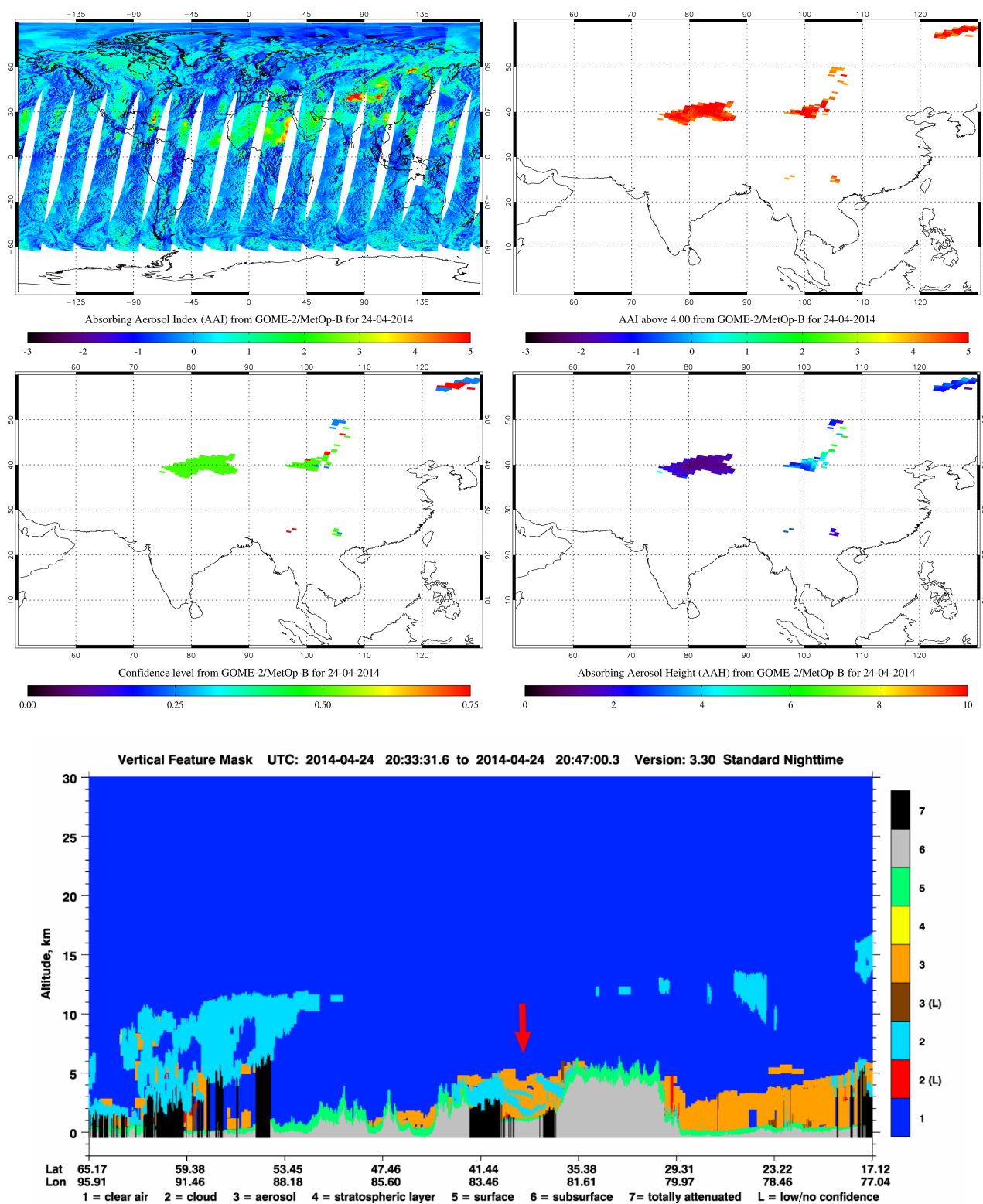
Figure 5: Top row: Global image of AAI and image of AAI above 4.0 index points for the region of interest. Data are from 24 April 2014. Middle row: Image of AAH and confidence level. Bottom row: CALIOP vertical feature mask. The arrow indicates the relevant geographical location.
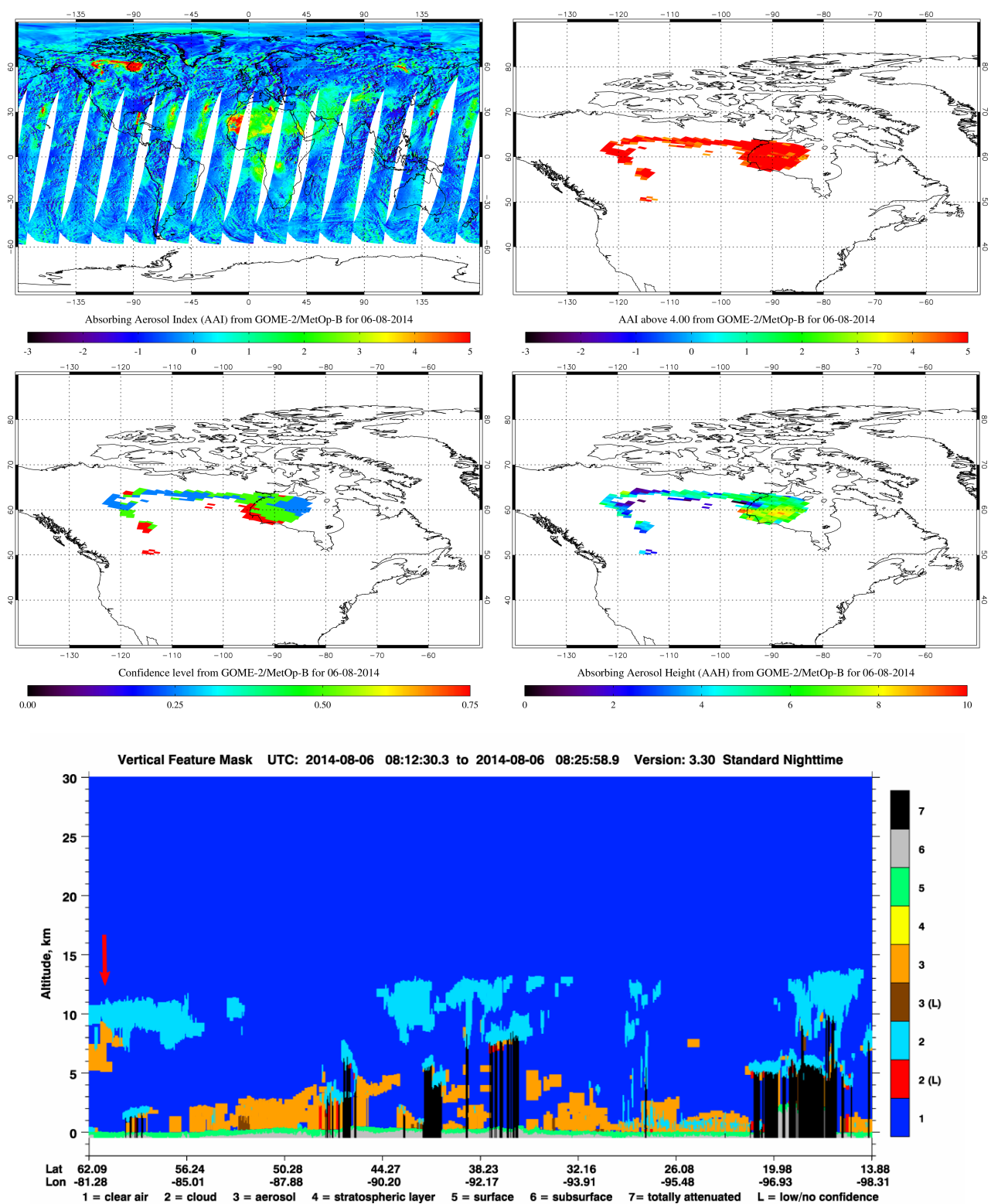
Figure 6: Top row: Global image of AAI and image of AAI above a threshold value of 4.0 for the region of interest. Data are from 6 August 2014. Middle row: Image of AAH and confidence level. Bottom row: CALIOP vertical feature mask. The arrow indicates the relevant geographical location.

3.1.5   Case V: Smoke from forest fires in Australia

The fourth case we study is the case of smoke from forest fires in Australia in the year 2009. The images are presented Figure 7, in the same manner as before. The data presented were recorded on 7 February 2009. In the regional AAI plot (upper row, second plot) the forest fires are located in the neighbourhood of the westernmost tail of the smoke plume. The smoke from the forest fires continued to travelled eastward in the direction of New Zealand.

The AAH plot (middle row) shows that the smoke plume reached altitudes between 6 and 10 km. In the CALIOP vertical feature mask (bottom row) we find the aerosol layer to be located at heights ranging between 5 and 9 km. This is a fair agreement between the GOME-2 AAH product and the CALIOP vertical feature mask. Note that the CALIOP results are reliable, but that the time difference between the GOME-2 and CALIOP measurements is large. Also note that as the aerosol concentration drops (AAI values lower than four) we see that the aerosol layer height drops as well.

3.2   Comparison with MISR Plume Height

In this section we compare the retrieved AAH product with the MISR Plume Height product. This product is based on MISR data in combination with MODIS data. The plume height product is available for a large number of interesting cases and can be obtained via the following URL:

https://misr.jpl.nasa.gov/getData/accessData/MisrMinxPlumes2/

The following cases were studied:

– Eyjafjallajökull volcanic eruption (Iceland)
– Smoke from forest fires in Southeast Asia

The MISR Plume Height product was developed and created in the framework of the MISR Plume Height Project. More information about the product can be found via the following URL:

http://misr.jpl.nasa.gov/getData/accessData/MisrMinxPlumes2/productDescription/

3.2.1   Case I: Eyjafjallajökull volcanic eruption

The series of volcanic eruptions of the Eyjafjallajökull volcano during April and May 2010 led to the closure of most of the European airspace in that period. In Figure 8 we investigate the situation as it was recorded on 13 May 2010. In the top row we present the AAI above a threshold value of 3.0 index points, and the retrieved AAH product. In the middle row we present the AAH confidence
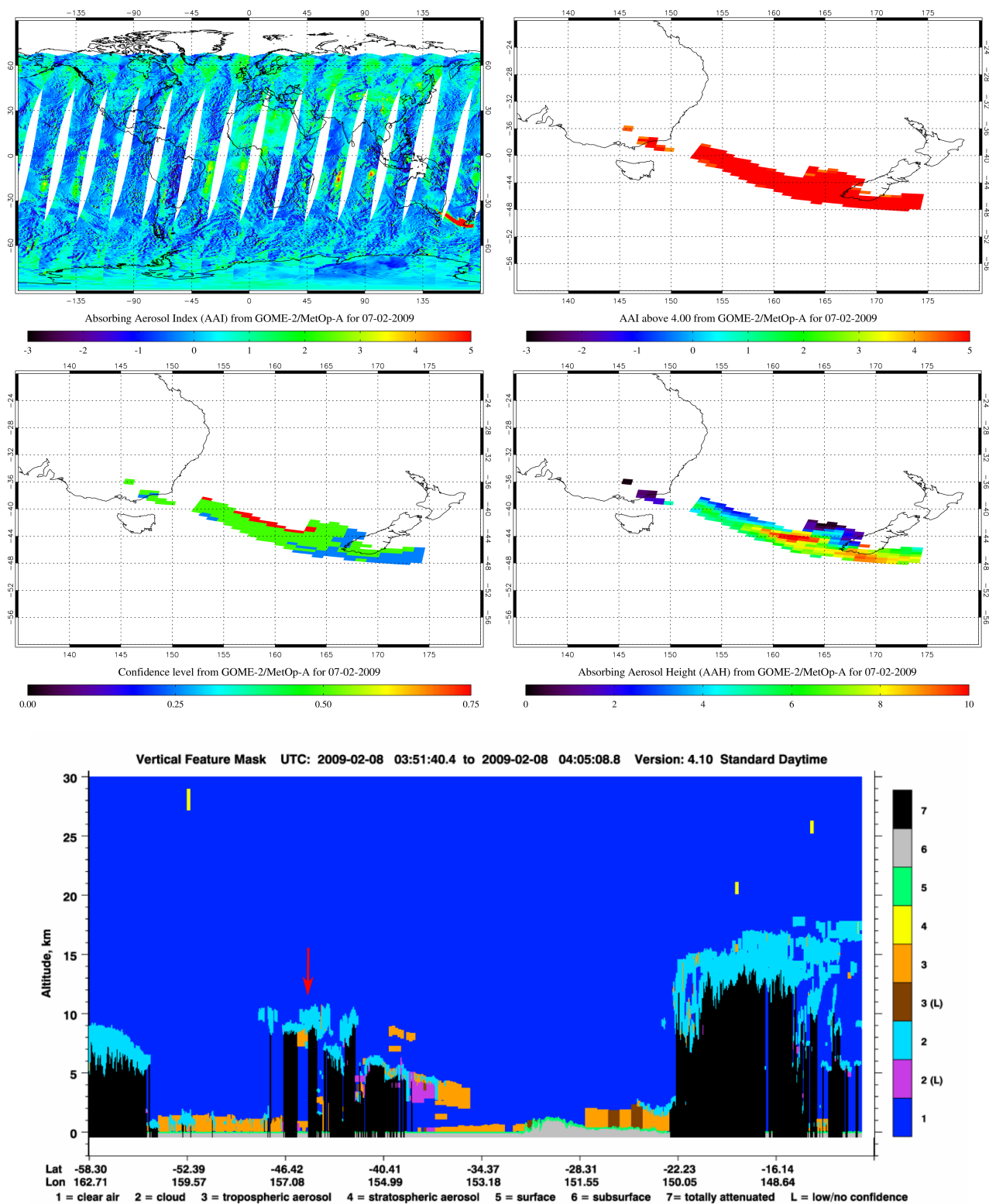
Figure 7: Top row: Global image of AAI and image of AAI above a threshold value of 4.0 for the region of interest. Data are from 7 February 2009. Middle row: Image of AAH and confidence level. Bottom row: CALIOP vertical feature mask. The arrow indicates the relevant geographical location.

level and a MISR image of the part of the ash plume that was selected for processing by the MISR plume height retrieval algorithm. The bottom row of Figure 8 presents the geographical location of the MISR granule from which the MISR plume height image originates, and the retrieved MISR plume height. The last image shows MISR plume height as a function of distance.

The AAH retrieval reports plume heights of 2 km or higher, with some outliers up to 4–5 km. The MISR plume height image shows heights of 2–3 km, and around 4–5 km. At first sight, this is a rather good agreement. However, the MISR plume height also reports the presence of clouds in parts of the ash plume. It is not clear if the AAH algorithm is mostly sensitive to the cloud or to the aerosol layer. In any case, the AAI is above 3 index points, which indicates that there is definitely (absorbing) aerosol contained in the scene. Note that the footprint size of the GOME-2 measurements is much larger than the spatial resolution of the MISR plume height product.

From the comparison with MISR we conclude that the AAH retrieval is about right for this one case of a volcanic plume. In the next section we will investigate the behaviour for a forest fire event.

3.2.2   Case II: Smoke from forest fires in Southeast Asia

The second case is one of a modest smoke plume caused by forest fires in Southeast Asia, observed on 26 March 2009. The results are presented in Figure 9. The AAI values found are smaller than 4.0 index points, which is the reason why the threshold value in the AAI plot was lowered to 2.0 index points. Note that this is lower than the threshold value used by the algorithm. The smoke plume is located near the coast. A feature with high AAI values over the ocean is observed also. This feature does not correspond to aerosol in the scene, but is actually caused by failing sun glint screening. Sun glint is filtered out in the images, but in this case a small island causes the sun glint filtering to fail.

Note that the plume in the MISR images extends over only 40–50 km. The plume shown in the AAH image extends over roughly 200 km. It is therefore hard to pin point the exact location of the plume, especially because of the time differences between the overpasses of the instruments involved. From the MISR plume height images we find aerosol heights between 2 and 4–5 km, and an outlier towards 6 km. The AAH product, however, shows layer heights ranging between 1 and 3 km and an outlier towards 6 km. The level of agreement is therefore not very high. This is an indication that the algorithm works less well for the thinner aerosol plumes.

3.3   Summary

Verification of the GOME-2 AAH product is not straightforward because of the limited number of aerosol height products currently available. Next to this, the AAH product by definition only makes
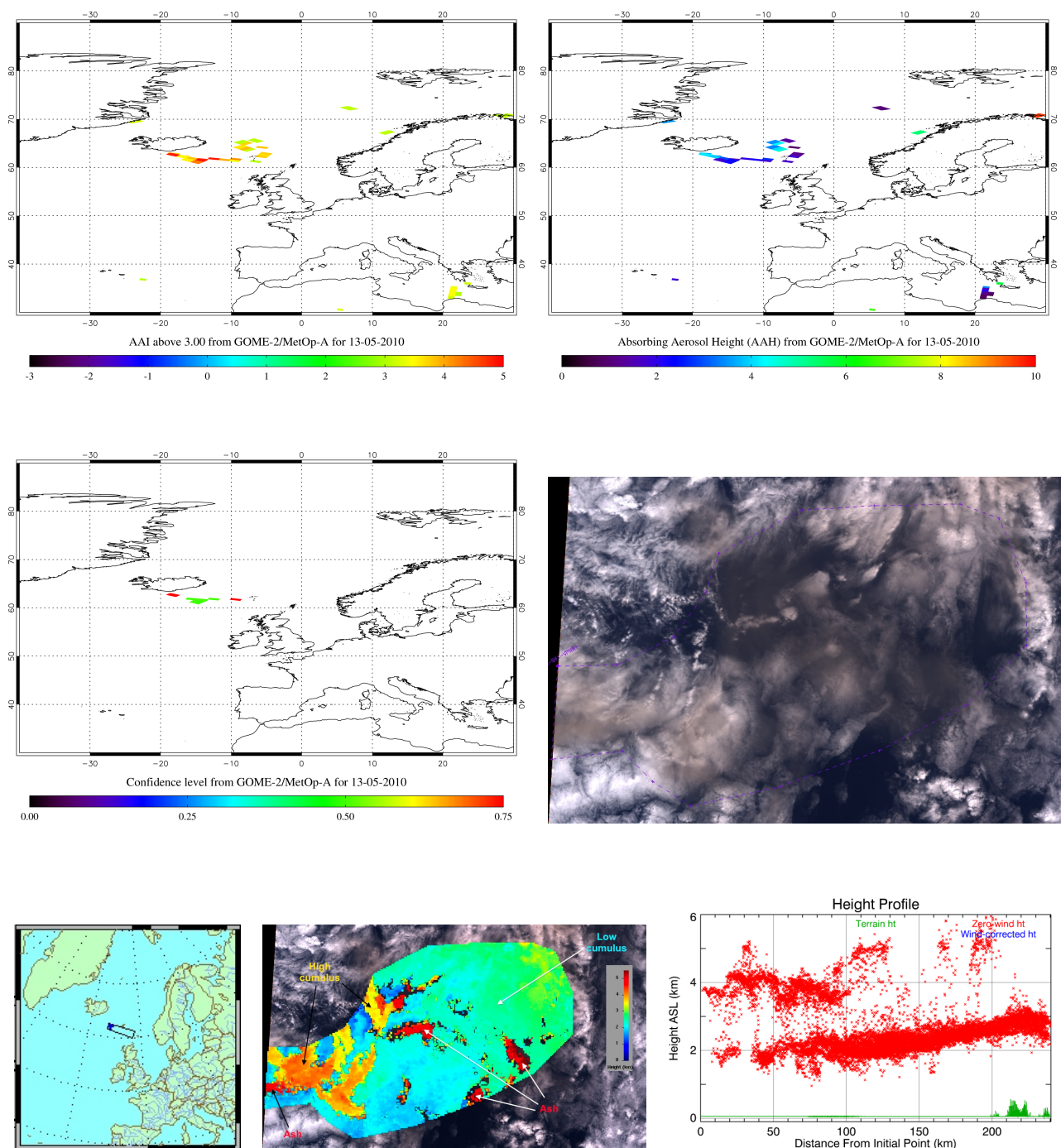
Figure 8: Top row: Global image of AAI above a threshold value of 3.0 index points and of AAH for the region of interest. The data are from 13 May 2010. Middle row: AAH confidence level and MISR image of part of the ash plume, to the east of Iceland. Bottom: Geographical location of the MISR granule, MISR plume height and plume height as a function of distance from the initial point.

Figure 9: Top row: Global image of AAI above a moderate threshold value of 2.0 index points and of AAH for the region of interest. The data are from 26 March 2009 and the smoke plume is near the coast. Middle row: AAH confidence level and MISR image of part of the smoke plume. Bottom: Geographical location of the MISR granule, MISR plume height, and p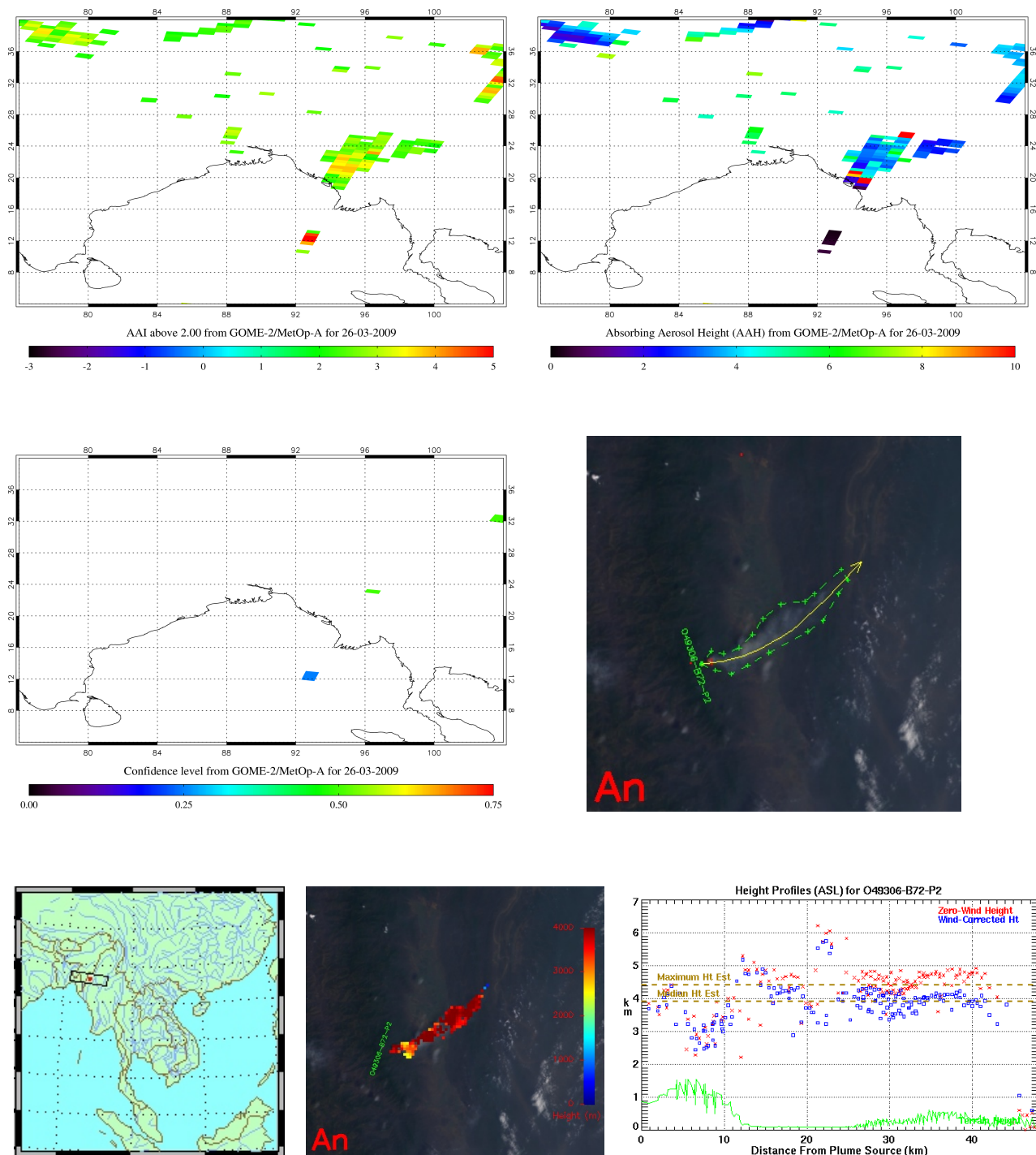lume height as a function of distance from the initial point (leftmost point of the smoke plume, where the fire is located).

sense for the subset of scenes that contain aerosols, and in practice only for scenes with a sufficiently high concentration of aerosols. When comparing aerosol height products from different sensors, the collocation (in space and time) needs to be sufficiently good, which is a challenge.

In this section we compared the GOME-2 AAH product with the aerosol height measured by the CALIOP instrument onboard the CALIPSO satellite. It is hard to find a good collocation, but when such a collocation is found, the comparison is quite meaningful, because the CALIOP measurements are very accurate. We presented a number of case studies, for volcanic ash, desert dust, and smoke from forest fires. For the case studies that we presented we found, despite the difficulties, rather good agreement between the CALIOP measurements and the GOME-2 AAH product.

The comparison with the MISR plume height product seems to be less successful. Again it was hard to find good collocations, this time because of the limited number of cases available via the URL mentioned earlier. The comparisons do not show a very good agreement, but, also do not show that the algorithm is failing. The main conclusion from these analyses is that the comparison itself is not very reliable. For the validation of the AAH product we therefore propose to use CALIOP data.

4 Proposed validation

For the validation of the retrieved GOME-2 AAH product we propose comparison with measurements performed by the CALIOP lidar as presented in section 3.1. Also ground-based lidar systems may be used provided that decent collocations (in space and time) can be found.

Another possible way of doing the validation is to use dispersion models which are able to follow the transport, evolution, and height of aerosol plumes.

A   Overview of solar eclipse events

The following two tables provide an overview of the major solar eclipse events that have occurred since the launch of MetOp-A and MetOp-B. The second column lists the dates on which the solar eclipse events occurred. The third and fourth columns together define the time intervals in which the measurements were noticeably affected. Data in these time intervals are not used.

satellite	date	start time	end time
MetOp-A	19-03-2007	02:48:52 UTC	03:05:09 UTC
MetOp-A	11-09-2007	11:17:10 UTC	11:23:52 UTC
MetOp-A	11-09-2007	12:51:33 UTC	13:06:19 UTC
MetOp-A	07-02-2008	03:11:08 UTC	03:21:21 UTC
MetOp-A	01-08-2008	03:16:39 UTC	03:22:45 UTC
MetOp-A	01-08-2008	08:18:26 UTC	08:24:26 UTC
MetOp-A	01-08-2008	09:59:50 UTC	10:20:20 UTC
MetOp-A	01-08-2008	11:42:59 UTC	11:49:24 UTC
MetOp-A	01-08-2008	13:24:03 UTC	13:30:31 UTC
MetOp-A	01-08-2008	15:04:20 UTC	15:13:01 UTC
MetOp-A	26-01-2009	05:55:33 UTC	06:10:45 UTC
MetOp-A	22-07-2009	01:07:56 UTC	01:23:31 UTC
MetOp-A	15-01-2010	05:19:17 UTC	05:33:47 UTC
MetOp-A	11-07-2010	17:50:19 UTC	18:02:31 UTC
MetOp-A	04-01-2011	08:00:51 UTC	08:18:07 UTC
MetOp-A	25-11-2011	06:38:19 UTC	06:48:26 UTC
MetOp-A	20-05-2012	14:46:28 UTC	14:53:47 UTC
MetOp-A	20-05-2012	16:28:10 UTC	16:35:10 UTC
MetOp-A	20-05-2012	18:09:10 UTC	18:15:10 UTC
MetOp-A	20-05-2012	23:26:31 UTC	23:41:02 UTC
MetOp-A	13-11-2012	21:05:02 UTC	21:22:45 UTC
MetOp-A	09-05-2013	23:16:45 UTC	23:35:28 UTC
MetOp-A	03-11-2013	11:38:12 UTC	11:56:10 UTC
MetOp-A	29-04-2014	04:16:10 UTC	04:23:05 UTC
MetOp-A	23-10-2014	21:09:51 UTC	21:23:16 UTC
MetOp-A	20-03-2015	09:57:13 UTC	10:13:58 UTC
MetOp-A	13-09-2015	06:05:18 UTC	06:18:25 UTC
MetOp-A	09-03-2016	01:02:19 UTC	01:18:35 UTC
MetOp-A	01-09-2016	07:10:12 UTC	07:26:21 UTC

MetOp-A	26-02-2017	12:42:51 UTC	12:54:12 UTC
MetOp-A	21-08-2017	16:43:30 UTC	16:52:37 UTC
MetOp-A	11-08-2018	06:00:00 UTC	24:00:00 UTC
MetOp-A	12-08-2018	00:00:00 UTC	18:00:00 UTC

Table 2: Solar eclipse events since the launch of MetOp-A. Given are the date and the time interval in which the measurements were noticeably affected.

satellite	date	start time	end time
MetOp-B	09-05-2013	22:32:29 UTC	22:52:41 UTC
MetOp-B	03-11-2013	10:55:02 UTC	11:04:14 UTC
MetOp-B	29-04-2014	05:06:27 UTC	05:18:55 UTC
MetOp-B	23-10-2014	20:23:24 UTC	20:35:23 UTC
MetOp-B	20-03-2015	09:15:23 UTC	09:32:35 UTC
MetOp-B	20-03-2015	10:49:31 UTC	10:58:55 UTC
MetOp-B	13-09-2015	07:06:24 UTC	07:17:31 UTC
MetOp-B	09-03-2016	00:17:31 UTC	00:33:49 UTC
MetOp-B	01-09-2016	08:01:54 UTC	08:19:56 UTC
MetOp-B	26-02-2017	13:34:21 UTC	13:58:24 UTC
MetOp-B	21-08-2017	17:29:51 UTC	17:47:36 UTC
MetOp-B	15-02-2018	20:09:15 UTC	20:15:46 UTC
MetOp-B	11-08-2018	08:03:23 UTC	08:11:41 UTC
MetOp-B	11-08-2018	09:44:23 UTC	09:58:12 UTC

Table 3: Solar eclipse events since the launch of MetOp-B. Given are the date and the time interval in which the measurements were noticeably affected.

References

Anderson, G. P., S. A. Clough, F. X. Kneizys, J. H. Chetwynd, and E. P. Shettle (1986), AFGL atmospheric constituent profiles (0–120 km), *Environ. Res. Pap. 954, Rep. AFGL-TR-86-0110*, Air Force Geophys. Lab., Hanscom AFB, Mass.

Danielson, J. J. and D. B. Gesch (2011), Global multi-resolution terrain elevation data 2010 (GMTED2010), *U.S. Geological Survey Open-File Report 2011-1073*, U.S. Geological Survey (USGS) and National Geospatial-Intelligence Agency (NGA), 26 p.

Koelemeijer, R. B. A., P. Stammes, J. W. Hovenier, and J. F. de Haan (2001), A fast method for retrieval of cloud parameters using oxygen a band measurements from the Global Ozone Monitoring Experiment, *J. Geophys. Res., 106*(D4), 3475–3490, doi:10.1029/2000JD900657.

Stammes, P., M. Sneep, J. F. de Haan, J. P. Veefkind, P. Wang, and P. F. Levelt (2008), Effective cloud fractions from the Ozone Monitoring Instrument: Theoretical framework and validation, *J. Geophys. Res., 113*, D16S38, doi:10.1029/2007JD008820.

Tilstra, L. G., O. N. E. Tuinder, and P. Stammes (2010), GOME-2 Absorbing Aerosol Index: statistical analysis, comparison to GOME-1 and impact of instrument degradation, in *Proceedings of the 2010 EUMETSAT Meteorological Satellite Conference*, EUMETSAT P.57, ISBN 978-92-9110-089-7, Cordoba, Spain.

Tilstra, L. G., O. N. E. Tuinder, P. Wang, and P. Stammes (2017), Surface reflectivity climatologies from UV to NIR determined from Earth observations by GOME-2 and SCIAMACHY, *J. Geophys. Res. Atmos., 122*, doi:10.1002/2016JD025940.

Trees, V., P. Wang, and P. Stammes (2020), Restoring the top-of-atmosphere reflectance during solar eclipses: a proof of concept with the UV Absorbing Aerosol Index measured by TROPOMI, *Atmos. Chem. Phys. Discuss.* [preprint], doi:10.5194/acp-2020-1172, in review.

Tuinder, O. N. E. and L. G. Tilstra (2016), Near Real-Time, Offline and Data Set Aerosol Products – Product User Manual, Doc. No. O3MSAF/KNMI/PUM/002, Issue 1.61, 11 January 2016, KNMI, De Bilt, The Netherlands.

Wang, P., P. Stammes, R. van der A, G. Pinardi, and M. van Roozendael (2008), FRESCO+: an improved O_2 A-band cloud retrieval algorithm for tropospheric trace gas retrievals, *Atmos. Chem. Phys., 8*(21), 6565–6576, doi:10.5194/acp-8-6565-2008.

Wang, P., O. N. E. Tuinder, L. G. Tilstra, M. de Graaf, and P. Stammes (2012), Interpretation of FRESCO cloud retrievals in case of absorbing aerosol events, *Atmos. Chem. Phys., 12*(19), 9057–9077, doi:10.5194/acp-12-9057-2012.